Published in Int. J. Coal Geology, 2021, 237, 103705, doi: org/10.1016/j.coal.2021.103705

Comparison of the Impact of Moisture on Methane Adsorption and Nanoporosity for Over Mature Shales and their Kerogens

Wei Li[a], Lee A. Stevens[a], Clement N. Uguna[a], Christopher H. Vane[b], Will Meredith[a], Ling Tang[c], Qianwen Li[d], Colin E. Snape*[a]

a. University of Nottingham, Low Carbon Energy and Resources Technologies Group, Faculty of Engineering, Energy Technologies Building, Triumph Road, Nottingham NG7 2TU, UK.
b. British Geological Survey, Centre for Environmental Geochemistry, Keyworth, Nottingham NG12 5GG, UK.
c. State Key Laboratory of Petroleum Resources and Prospecting, China University of Petroleum, Beijing 102249, China.
d. Sinopec Petroleum Exploration and Production Research Institute, Beijing 100083, China.

* Corresponding author, Colin.Snape@nottingham.ac.uk

Abstract

Moisture in shales under reservoir conditions adversely affects gas adsorption and nanoporosity and is also likely to impact on the contribution that kerogen makes to the methane adsorption capacity. To investigate these phenomena, two over mature shales from the Wufeng-Longmaxi Formation, south of the Sichuan basin, and their kerogens isolated by demineralisation were investigated dry and at 95% relative humidity (R.H.) by high-pressure methane adsorption, and low-pressure nitrogen (N_2) and carbon dioxide (CO_2) sorption. The kerogen concentrates account for 68-97% and 50-64% of the methane adsorption capacities for the shales dry and at 95% R.H. respectively. However, the isolated kerogens could adsorb more methane than the organic matter in the shales because their shallower adsorption isotherms indicate large micropores and small mesopores not evident for the shales. Methane adsorption capacities of the kerogens and shales reduced by 46-72% at 95% R.H.. This compares with the reductions in surface area (SA) and pore volume of 81% and 48-59%, respectively, for the kerogens and 98-99% for both SA and pore volume of the shales at 95% R.H.. Water can block most micropores less than 1.3 nm reducing the micropores volume and blocking the micropore necks connecting the larger pores, and vastly reducing accessible pores for gas transport. The greater proportional losses in SA and pore volume compared to

the methane adsorption capacities is probably due to ice forming at -196 °C in the low-pressure N_2 analysis. Failure to take moisture into account for free and adsorbed methane overestimates the total gas in place (GIP) by 36-45% for the shales investigated.

Keywords: Kerogen; Moisture; Methane Adsorption Capacity; Nanoporosity.

1. Introduction

Shale gas is stored in adsorbed, free and dissolved states and it is often estimated from the sum of the adsorbed and free gas in the pores (Chen et al., 2017; Curtis, 2002; Jarvie et al., 2007; Rexer et al., 2014; Ross and Bustin, 2008). The adsorbed gas can be significant under reservoir conditions, estimated as 20-85% of the total gas in organic-rich shales (Adesida et al., 2011; Curtis, 2002; Heller and Zoback, 2014; Ross and Bustin, 2008). Kerogen, the organic matter insoluble in alkali, non-oxidizing acids and organic solvents in shales (Durand, 1980; Hunt, 1979), is considered to store much of the gas since methane adsorption capacity of shale generally increases with increasing total organic content (TOC) (Gasparik et al., 2014; Ross and Bustin, 2009; Zhang et al., 2012). In addition to the kerogen, the major minerals in shales including quartz, clays and calcite are also believed to provide porosity for shale gas to adsorb in different extents (Gasparik et al., 2014; Gasparik et al., 2012; Loucks et al., 2012; Ma et al., 2017; Peng et al., 2020; Peng et al., 2019; Ross and Bustin, 2009). Gasparik (2012) reported no correlation between TOC and dry adsorption capacity for some shales, suggesting that the sorption capacities of the minerals can be significant.

To investigate methane adsorption on isolated kerogens, Hu (2014) chose two kerogens of different maturity (vitrinite reflectance (VR) of 0.58 and 2.01% Ro), and found that the more mature kerogen had a much higher adsorption capacity. Methane adsorption experiments on organic-rich shales and their isolated kerogens were conducted at different temperatures under dry conditions to study the impact of different parameters on gas adsorption but not including moisture (Li et al., 2018; Rexer et al., 2014; Zhang et al., 2012). Fan (2014) found that 43-57% of the methane adsorption in dry shales was accounted for by the kerogen, confirming that kerogen has a much larger methane adsorption capacity than minerals. Rexer et al (2014) compared kerogen and shale using low-pressure nitrogen (N_2) and carbon dioxide (CO_2) and high-pressure methane isotherms and identified that the vast majority sorption of methane occurs in the pores less than 6 nm, and kerogen accounts for about 50% total measured adsorbed methane in dry shales investigated. Although these studies confirm that kerogen accounts for much of the methane adsorption capacity in shale, the impact of moisture present has not been addressed.

Moisture always exists under reservoirs conditions and has a profound negative influence on gas adsorption capacity (Heller and Zoback, 2014; Ji et al., 2012; Jin and Firoozabadi, 2014;

Zolfaghari et al., 2017b). Some studies have addressed the impact of moisture on methane adsorption for shales and coals (Gasparik et al., 2014; Joubert et al., 1973; Ross and Bustin, 2007; Weniger et al., 2012; Whitelaw et al., 2019; Zou et al., 2018). Joubert (1973) found methane adsorption capacity for coals decreased with increasing humidity, although there was a "critical value" of moisture above which no change in adsorption capacity occurred. High critical values were thought to relate to high coal oxygen contents since there is a strong interaction between the polar water molecule and the surface oxygen complexes (Day et al., 2008; Joubert et al., 1973). The critical moisture content of shale is approximately 75% R.H. (Gasparik et al., 2014). Ross and Bustin (2007) compared the isotherms of dry shales with moisture equilibrated shales from the Lower Jurassic Gordondale Member and showed that methane adsorbed in dry shales (0.5–4.0 cm^3/g) were much larger than that in moisture equilibrated shales (0.1–1.6 cm^3/g). Reductions of 20-85% in methane adsorption capacities have also been reported by Merkel (2016) and Whitelaw et al (2019) at high R.H., the latter finding that moisture reduced pore volume by over 90%. In contrast, Zou (2018) reported much smaller reductions of less than 20% in methane adsorption capacity and 30% in pore volume because their degassing of the 84% R.H. shales and standardised pre-evacuation procedures for the low and high-pressure instruments is likely to have removed any free and weakly adsorbed water, resulting in the moisture being considerably less than 84% R.H. when the experiments started. Moisture adsorbed on hydrophilic clay minerals is considered to be main reason for the decreasing methane adsorption in a number of studies (Heller and Zoback, 2014; Jin and Firoozabadi, 2014; Liming et al., 2012a; Zolfaghari et al., 2017a; Zou et al., 2018).

Methane adsorption in shale and kerogen is clearly related to pore structure, mainly pore surface area (Li et al., 2019; Liming et al., 2012b; Rexer et al., 2014). Molecular simulation was used to study the impact of different pore sizes on methane adsorption and other gases (e.g. CO_2, N_2) in kerogen (Huang et al., 2018; Xiong et al., 2017; Zhao et al., 2018). In addition to molecular simulation, some experimental studies on kerogens have focused on methane adsorption, but without investigating the pore size distribution (PSD) (Fan et al., 2014; Hu, 2014; Li et al., 2018; Pang et al., 2019; Zhang et al., 2012). Other studies have only addressed pore characterization without considering methane adsorption (Adesida et al., 2011; Cao et al., 2015; Chen et al., 2013; Ji et al., 2017; Liu et al., 2018). Only a few studies (Rexer et al.,

2014; Xiong et al., 2017) have investigated both methane adsorption and pore structure but only under dry conditions.

This study is the first to relate methane adsorption capacities and pore characteristics of shales and their isolated kerogens, both dry and equilibrated at 95% R.H., and to compare the impact of moisture on methane adsorption capacity and nanoporosity for kerogens and shales. Furthermore, this research provides new guidance on accounting for moisture to estimate gas in place (GIP) for shales. This is often estimated from the total amount of free gas obtained from the total porosity and adsorbed gas content measured from methane adsorption (Li et al., 2018; Tang et al., 2016). GIP based on the accessible pore volume and methane adsorption of dry shales without taking moisture into account is overestimated (Li et al., 2018; Tang et al., 2016), since moisture exists in shale reservoirs (Feng et al., 2018; Loucks and Ruppel, 2007; Merkel et al., 2015).

2. Geological setting

Sichuan Basin is a marine–continental complex superimposed basin located in the south of China. As a hydrocarbon-abundant basin it contains promising shale gas resources (Tang et al., 2019; Zou et al., 2010; Dai et al., 2014). The study area is situated in the south part of Sichuan Basin (Figure 1A), well developing the Upper Ordovician Wufeng Formation and Lower Silurian Longmaxi Formation shale (Figure 1B) (Dai et al., 2014). Wufeng-Longmaxi Formation containing substantial high-quality shale is the main target for shale gas exploration in Sichuan (Dong et al., 2018; Tang et al., 2019). Normally, huge thickness, rich organic matter and high maturity shale are the characteristic of Wufeng-Longmaxi Formation shale (Dong et al., 2018; Dongjun et al., 2016; Fan et al., 2014).

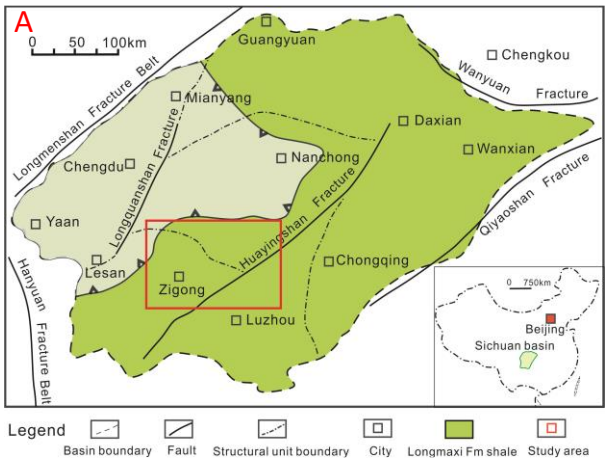

Chronostratigraphic			Lithostratigraphic			Thickness (m)	Sedimentary environment
Eonthem	Erathem	System	Formation	Member	Code		
Lower Paleozoic	Silurian	Lower	Longmaxi	Upper	S_1l	0~450	Continental shelf
				Lower			
	Ordovician	Upper	Wufeng		O_3W	5~25	Continental shelf
		Middle	Linxiang Baota		O_2b	20~80	Continental shelf
		Lower	Dachengsi		O_1d	131~280	Restricted marine -mudflat
			Lyuohanpo		O 1		
	Cambrian	Mid-Upper	Xixiangchi		$€_{2-3}$	191~259	Restricted marine -tidal flat
		Lower	Yuxiansi		$€_1y$	212~246	Restricted marine -intertidal
			Jiulaodong		$€_1j$	409~514	Open marine -continental shelf
Neoproterozoic	Sinian	Upper	Dengying	4th	Z_2dn	0~400	
				3rd		0~70	Restricted marine -tidal flat
				2nd		300~1000	
				1st		30~500	

B

Figure 1. A) The location of the study area in Sichuan Basin, B) Stratigraphic column of Sichuan Basin, modified from Dai (2014).

3. Methods

Two shale samples, Shale 1 (SH1) and Shale 2 (SH2) from different wells with a depth of 4119 and 4098 m in the study area of Wufeng-Longmaxi Formation, Sichuan Basin, China were selected for kerogen isolation. Dry and moisture-equilibrated kerogen concentrates and shales were prepared for the high-pressure methane adsorption, low-pressure gas sorption, and Helium pycnometry for the methane adsorption capacity, pore texture, and skeletal density. Dry shales are prepared for the vitrinite reflectance, elemental analysis, X-ray diffraction, field emission scanning electron microscopy (FE-SEM), and mercury intrusion porosimetry (MIP) to obtain the maturity, TOC, mineral composition, visible pore structure, and bulk density. The flowchart of these experiments (Figure S1) is in Supplementary material.

3.1 Sample preparation

3.1.1 Kerogen isolation The two kerogen concentrates, K1 and K2 isolated from SH1 and SH2, respectively, were prepared by standard demineralisation procedures (Guthrie and Pratt, 1994; Rexer et al., 2014). Shale samples (60 g each) crushed into powder (<250 µm) and treated with 37% hydrochloric acid (HCl) at 25 °C for 12 hours to remove carbonates. The HCl treated shales were washed with distilled water before using 40% hydrofluoric acid treatment at 25 °C for 48 hours to remove aluminosilicate minerals. Samples were washed with distilled water and treated with 37% HCl again to make sure to remove the fluorapatites which can precipitate after HF treatment (Guthrie and Pratt, 1994). After decanting the acid, the powdered residue was then repeatedly washed six times with distilled water to remove the acid and reach pH 7. Samples were then freeze-dried (−5 °C) for 6 hours and dried at ambient temperature. After drying, 7.21 and 6.55 g of K1 and K2 were obtained respectively from 60 g of shale, and the yield of kerogen concentrate can be calculated.

3.1.2 Moisture-equilibration method The adsorption capacity of shale is influenced by particle size, where milling can destroy or create pores in shale (Gasparik et al., 2014; Rexer et al., 2014). Thus, shale samples were crushed into particles with a size range of 2-4 mm (10-5 mesh), but not to powders so as not to disrupt the interconnectivity between macro, meso and micropores (Whitelaw et al., 2019). The kerogen concentrates were in powder form after isolation with a particle size <250 µm. The shales and kerogen concentrates were first dried at 120 °C in a vacuum oven (<0.5 mbar) for 48 hours to get the dry sample and dry mass. Then, the 95±2% R.H. moisture equilibrated (wet) samples were prepared in a vacuum desiccator containing pre-stirred saturated potassium nitrate (KNO_3) solution (8 g KNO_3/10 mL H_2O) at a controlled temperature of 20 °C for 48 hours (Young, 1967; Zolfaghari et al., 2017a). A logger in the desiccator was used to monitor the R.H. and the temperature (Figure S2). The moisture content for the wet samples were calculated from the mass difference (equation (1)) of equilibrated 'wet' samples and after drying under vacuum. The water volume uptake in shales at 95 % R.H. are calculated from the moisture contents and densities by equation (2).

$$W = \frac{M_{water}}{M_{dry}} \quad (1)$$

$$S_w = \frac{V_{water}}{V_{dry\ pore}} = 1 - \frac{\rho_{dry\ sk}}{\rho_{dry\ sk} - \rho_{dry\ bulk}} + \frac{\rho_{dry\ sk} \times \rho_{dry\ bulk} \times (1+W)}{\rho_{wet\ sk} \times (\rho_{dry\ sk} - \rho_{dry\ bulk})} \quad (2)$$

Where, W is the moisture content, M_{dry} is the mass of dry sample, M_{water} is the mass of the water, S_w is the water volume uptake, V_{water} is the volume of the water in pore, $V_{dry\ pore}$ is the total pore volume in dry sample, $\rho_{dry\ bulk}$ is the bulk density of the dry sample from mercury intrusion porosimetry (MIP) at 0.03 bar, $\rho_{dry\ sk}$ and $\rho_{wet\ sk}$ are the skeletal densities of the dry and wet samples obtained from helium pycnometry.

3.2 Vitrinite reflectance, Elemental analysis, and X-ray diffraction

Shale vitrinite reflectance (Ro) was obtained and converted from the reflectance of bitumen (Rb) by equation Ro = (Rb + 0.2443) / 1.0495 (Schoenherr et al., 2007) to indicate the maturity of shales, due to their high maturity vitrinite was not easy to observe. A LEICA DM4500P microscope was used for reflectance measurement on the prepared polished shale particle (2-4 mm) block. Measurement was carried out in non-polarized light at a wavelength of 546 nm in oil immersion and the data were collected via the Hilgers Fossil Man system connected to the LEICA DM4500P microscope. TOC contents were determined using Leco CHN628 instruments. Up to 3 g of the powdered shales (<250 µm) were treated using HCl with a concentration of 1 mol/L for 24 hours to remove carbonates. The samples were then washed with distilled water 6 times to remove the acid and reach pH 7. After carefully decanting the water from the samples, the samples were dried in the vacuum oven (<0.5 mbar) for 48 hrs at 120 °C. The TOC contents were measured using 120 mg shale and 75 mg kerogen, respectively. All the elemental analyses were carried out in triplicate. X-ray diffraction (XRD) method was used to determine the relative mineral phases using a Rigaku D/max-2500PC instrument, shale samples were ground into less than 0.04 mm powder, then loaded in the copper holders and scanned with the D/max-3B X-ray diffractometer with the scan angle from 5° to 90° at working voltage of 40 kV and current of 40 mA conditions.

3.3 Field emission scanning electron microscopy (FE-SEM)

The shales (2-4 mm) were analysed where one side surface of the selected sample was polished by argon-ion to get a smooth surface using a Leica EM TIC020 mill with an accelerating voltage of 8 kV, current of 2.8 mA for about 8 hours. Then, the samples were coated with a 25 nm conductive layer by the PELCO conductive carbon paste. The samples were imaged using a JSM-6700F FE-SEM, all the high-resolution FE-SEM images were processed using Image J-1.53a software (Abràmoff et al., 2004).

3.4 High-pressure methane adsorption

High-pressure methane adsorption measurements were performed using a Particulate Systems High-Pressure Volumetric Analyzer (HPVA-100) designed to obtain high-pressure sorption isotherms employing the static volumetric method (pressures up to 105 bar and temperatures up to 500 °C). Approximately 10 g of moisture equilibrated shale (2-4 mm) and 3 g of moisture equilibrated powder kerogen concentrate (<250 µm) were weighed and loaded into the 10 mL stainless steel sample cell and sealed. The helium volume calibration was done before analysis on an empty cell. For wet samples, the methane adsorption isotherms were acquired from 1.2 to 105 bar at 25 °C. Here, the external valve linking the analysis cell to the instrument manifold remained closed until the analysis or manifold pressure reaches 1.4 bar, then opened, the pressure settles to 1.2 bar, avoiding samples being subjected to a vacuum on the high-pressure instrument. The mass deviation of wet samples before and after analysis was less than ±0.0018%, verifying the moisture is still in the sample. For dry adsorption isotherms, the samples were degassed at 120 °C for 48 hours before starting the methane adsorption method. A sample pre-evacuation was carried out for 45 minutes to reach a vacuum setpoint of 0.013 bar on the high-pressure instrument and an isotherm was generated from 0 to 105 bar. Similar free space (void volume) corrections were carried out on this instrument as for the low-pressure gas sorption method (3.5) and blank correction carried out on both dry and wet sample data.

Each sample was analysed in triplicate to assess errors. The excess adsorption quantity is obtained by the volumetric sorption measurement; therefore, it is necessary to convert to absolute adsorption quantity by Gibbs equation (equation (3)) (Sircar, 1999; Tang et al., 2016). The HPVA can measure the adsorption up to 105 bar, whereas, the adsorbed gas quantities at higher pressures can be predicted by the dual-site Langmuir model which is for heterogeneous adsorbents (Tang et al., 2016; Whitelaw et al., 2019). The equation for the dual-site Langmuir can be written in the following form (equation (4)), and equation (5) and (6) show the $b_1(T)$ and $b_2(T)$:

$$n_a = n_e + (V_a \times \rho_g) \quad (3)$$

$$n_a(P,T) = n_{max} \times \left[(1-\alpha)\frac{b_1(T)P}{1+b_1(T)P} + \alpha\frac{b_2(T)P}{1+b_2(T)P}\right] \quad (4)$$

$$b_1(T) = A_1 \times exp\left(-\frac{E_1}{RT}\right) \quad (5)$$

$$b_2(T) = A_2 \times exp\left(-\frac{E_2}{RT}\right) \quad (6)$$

Where, n_a is the absolute adsorption quantity; n_e is the excess adsorption quantity; V_a is the pore volume for gas to adsorb into; ρ_g is the density of the bulk gas; $n_{max}$is the maximum equilibrium adsorption quantity; $b_1(T)$ and $b_2(T)$ are the temperature-dependent equilibrium constants; $b_1(T)$ and $b_2(T)$ are weighted by a coefficient (α); α is the fraction of the second type of site ($0 < \alpha < 1$); E_1 and E_2 are the energy of adsorption of two sites; A_1 and A_2 are the pre-exponential coefficient; R is the ideal gas content, P is the pressure and T is the temperature.

3.5 Low-pressure gas sorption

Low-pressure gas sorption experiments were carried out for both dry and 95% R.H. moisture equilibrated (wet) samples by a Micromeritics Surface Area and Porosity Analyser (ASAP 2420). For shale samples, 4 g particles (2-4 mm) were used for the low-pressure N_2 sorption experiments, 2 g for CO_2 adsorption and about 1 g of the powdered kerogen concentrates (<250 μm) for both N_2 and CO_2 sorption. All the dry samples were degassed under high vacuum (<0.013 mbar) at 120 °C for 48 hours prior to analysis, and a pre-evacuation of 3 hours on the low-pressure instrument to reach the vacuum setpoint (0.013 bar) to start the isotherm. For low-pressure N_2 sorption, the prepared wet samples were frozen first in liquid N_2 for 30 minutes, before manually evacuating the sample tube and starting the analysis. This ensures moisture equilibrated samples are not exposed to vacuum at warmer temperatures on the low-pressure instrument. The mass deviation of wet samples before and after analysis was less than ±0.0020%, verifying the moisture still in the samples. The analysis for both dry and wet samples were performed in a liquid N_2 bath (-196 °C), with the relative pressure (P/P°, P is the absolute equilibrium pressure and P° is the saturation pressure) from 10^{-7} until 0.995 P/P°. CO_2 adsorption isotherms were acquired from 6×10^{-5} to 3.5×10^{-2} P/P° (absolute pressure is from 0.002 to 1.2 bar) at 0 °C to characterise the ultra-microporous structure (<0.8 nm) of dry shale and kerogen concentrates (Liu et al., 2015; Whitelaw et al., 2019). CO_2 adsorption was not carried out for wet samples because the experimental temperature is 0 °C which could not hold the moisture in the sample under low pressure.

Brunauer-Emmett-Teller (BET) theory was used to calculate the SA, where the P/P° between 0.05 and 0.2 of N_2 adsorption and P/P° between 0.025 and 0.030 of CO_2 adsorption were selected to get a positive BET 'C' parameter (Brunauer et al., 1938; Thommes et al., 2015). With the development of density functional theory and computer simulation approaches, the whole range of micro and mesopores can be probed with commercially available models such as Non-Local Density Functional Theory (NLDFT) (Qi et al., 2017; Rouquerol et al., 2007). NLDFT method based on the carbon slit pore model is applied to calculate the PSD from 0.33 to 100 nm in this study. Helium pycnometry was used to measure the skeletal density of wet and dry samples for the manual calculation of warm and cold free space to obtain exact gas sorption results, as the free space test by helium cannot be used during the low-pressure gas sorption experiment, because an automatic warm free space test on the instrument would expose the moisture equilibrated samples to a vacuum which would remove the moisture.

3.6 Mercury intrusion porosimetry

A Micromeritics Autopore IV Series instrument was used to obtain the bulk density and the porosity of dry shale samples. 2 g shale (2-4 mm) samples were vacuumed dry at a temperature of 120 °C for 48 hours in a vacuum oven (<0.5 mbar) and loaded into a 5 ml solid penetrometer 0.392 ml stem volume, then sealed. The intrusion of mercury was recorded from 0 to 4137 bar. The volume of mercury entering the shale pores at a given pressure can be converted to pore volume and size using the Washburn equation for slit/angular shaped pores. A contact angle of 151.5° and a surface tension of 475.5 mN/m for mercury intrusion in shale was used to provide a pore size distribution from 231 µm to 2 nm (Wang et al., 2016). Correction methods were applied by running a blank penetrometer to remove any intrusion detected from an empty penetrometer (Malik et al., 2016).

4. Results and discussion

4.1 TOC, maturity, mineral compositions, and moisture content

The TOC, maturity, compositions and physical properties of the two shales and their isolated kerogen concentrates are presented in Table 1. SH1 (5.1%) has a higher TOC than SH2 (2.4%). Combining the kerogen concentrate yields for SH1 and SH2 of 12.0 and 10.9 wt.%, respectively, with TOCs of 36.0 and 18.7%, indicates that the K1 and K2 account for 86% and 83% of the TOC in the SH1 and SH2, since K1 provides 4.4 wt.% TOC for SH1 (5.1 wt.%), and K2 provide 2.0 wt.% for SH2 (2.4 wt.%), indicating the demineralization process did not cause significant

kerogen weight loss. The Ro of SH1 and SH2 are 2.95 and 2.58%, suggesting the shales are all thermally over matured. XRD shows clay mineral content of SH1 (18.4%) is much lower than SH2 (35.8%), while the quartz content of 55.4% for SH1 is higher than that of 41.7% for SH2. For the 95% R.H. moisture equilibrated samples, the kerogen concentrates adsorb much more water (15.5 and 13.0 wt.%) than the shales (1.48 and 1.22 wt.%), due to their higher SA and pore volumes. Considering the yield, the moisture content provided by K1 and K2 (1.86 and 1.42 wt.%) for shales are even higher than the moisture content of SH1 and SH2, which could in part arise from demineralisation opening inaccessible pores in the shales or the moisture may not reach all organic matter pore in shale.

Table 1. TOC, maturity (Ro), mineral compositions and moisture contents of the shales.

Sample Name	Moisture (Wt.%)	TOC(Wt.%)	Ro(%)	Yield (wt.%)	Mineral (%)					
					Clay	Quartz	Plagioclase	Calcite	Dolomite	Pyrite
SH1	1.48±0.14	5.1±0.1	2.95	-	18.4	55.4	3.1	4	14.9	4.1
SH2	1.22±0.10	2.4±0.1	2.58	-	35.8	41.7	6.9	4.4	6.9	4.3
K1	15.5±2.9	36.3±1.4	-	12						
K2	13.0±1.2	18.7±0.2	-	10.9						

The mean of moisture content and TOC are from triplicate experiments (3.1.2) and (3.2), and the errors represent the dispersion of a dataset relative to its mean.

4.2 Pore structure from FE-SEM

FE-SEM can observe pores larger than 100 nm in shales (Loucks et al., 2012; Loucks et al., 2009; Milliken et al., 2013; Zou et al., 2010). As Figure 2 indicates that shale is heterogenous from composition to pore structure, there are more pores in the organic matter than the pores in the clay minerals. Figure 2 shows that the region of most organic matter is in the range of 5-20 µm, surrounded by minerals (Figure 2A) and a large number of macropores in the organic matter (Figure 2A). Intra-particle macropores in the organic matter are evident (Figure 2B, C) with irregular shapes (Figure 2B), with only a few pores larger than 500 nm (Figure 2D). The most minerals contain inter-particle pores (Figure 2C).

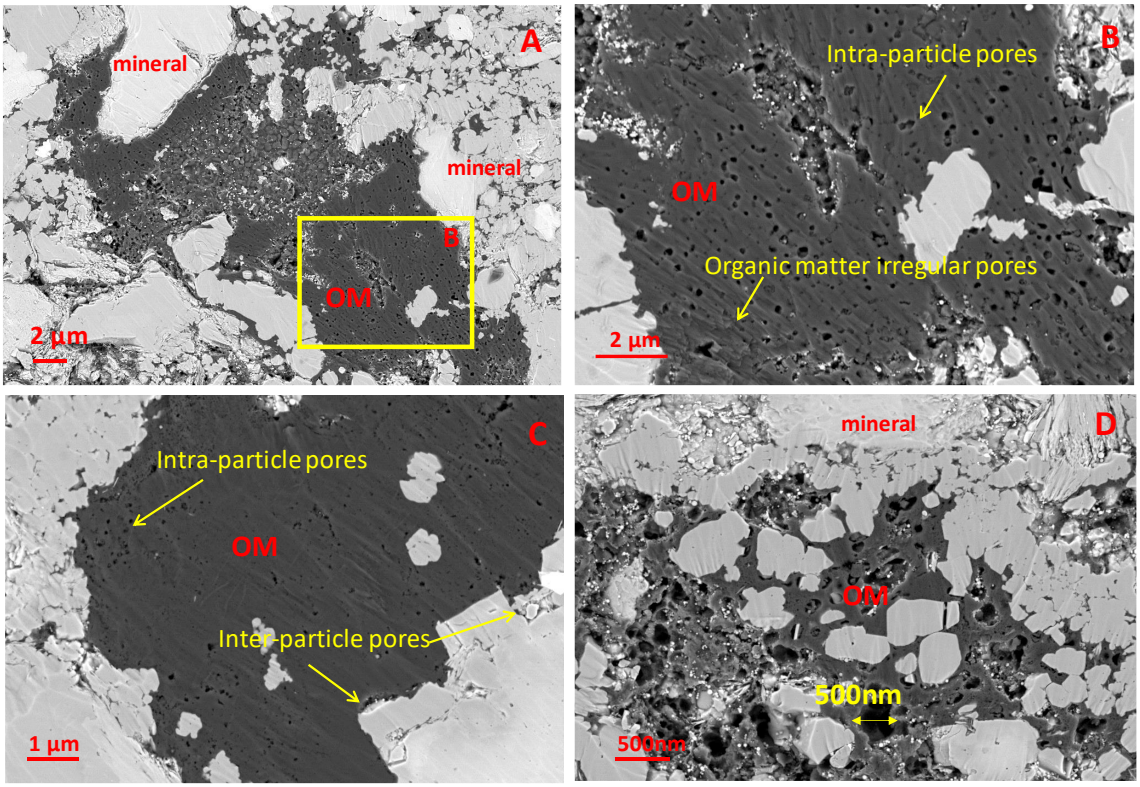

301

302 Figure 2. FE-SEM backscattered electron images of organic matter and macropores in shales.
303 A) Minerals and organic matter (OM) distribution in SH2, B) is the enlarged figure of A, OM
304 irregular pores in SH2, C) Intra-particle pores and inter-particle pores in SH1, D) The size of
305 OM pores in SH2.

4.3 Methane adsorption capacities of the shales and kerogen concentrates

4.3.1 Moisture impact on methane adsorption capacity Figure 3 indicates that the dry kerogen concentrates and shales have much higher methane adsorption capacities than their wet counterparts. Approximately 72 and 54% of the equilibrium methane adsorption capacities are lost for K1 and K2, respectively (K1 reducing from 22.2 mg/g to 6.2 mg/g, and K2 from 12.5 mg/g to 5.8 mg/g, Table 2). The same pattern is found for the shale samples, with approximately 50% of equilibrium methane capacities of the dry shales being lost (SH1 reducing from 2.7 mg/g to 1.5 mg/g, and SH2 from 2.0 mg/g to 0.98 mg/g wet, Table 2). The level of reduction for the shales is consistent with previous studies (Gasparik et al., 2014; Merkel et al., 2016; Whitelaw et al., 2019). A significant decrease in adsorption capacity of 40-60% was observed between the dry and moisture equilibrated shale samples studied by Gasparik et al. (2014). Merkel et al. (2016) found that Lacustrine shales lose 20-80% of initial dry adsorption capacity upon full moisture equilibration (97% R.H.). Whitelaw et al. (2019) also found that equilibrated methane adsorption amount dropped by 27% after the shale samples were equilibrated at 50% R.H..

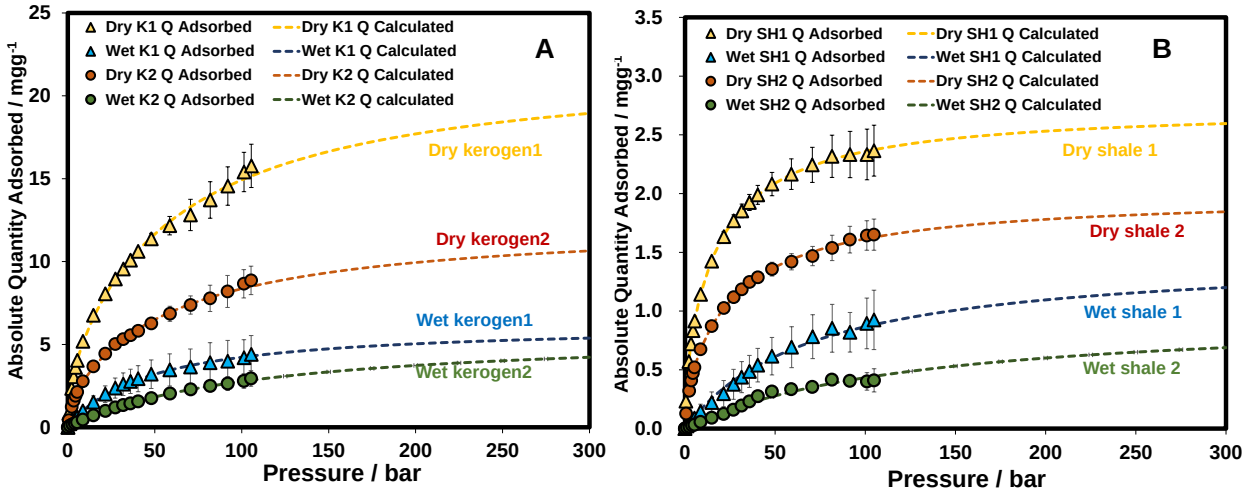

Figure 3. Comparison of absolute methane adsorption isotherms of dry and wet (95% R.H.) kerogen concentrates and shales at 25 °C. A) dry and wet kerogen concentrates, B) dry and wet shales. Each sample was analysed in triplicate by HPVA, the data points are the mean from triplicate experiments and the error bars represent the dispersion of a dataset relative to its mean. The fitting parameters for dual-site Langmuir model is in supplementary material table S1.

The dry shales have slightly steeper isotherms (Type 1a) than their kerogen counterparts (Type 1b) (Figure 3), suggesting that isolated kerogens have higher proportion of larger micropores and smaller mesopores, which can be accessed by demineralisation, as the steeper uptake at low pressure are mainly contributed by narrow micropores (<1 nm) (Thommes et al., 2015). The isotherm shapes of wet samples are less steep than the dry ones (Figure 3), indicating higher pressure and more energy are required to adsorb the same amount. This suggests that moisture preferentially reduces adsorption on the smaller micropores as intuitively expected, by blocking the accessible micropores, occupying/changing the adsorption sites or swelling clays (for shale) and blocking the access.

4.3.2 Contribution of kerogen concentrates to the methane adsorption capacities of the shales The methane adsorption capacities for the kerogen concentrates and corresponding shales are compared in Table 2, which lists the contributions of the kerogen concentrates made to methane adsorption capacities for the shales under dry and wet conditions. The contributions from the kerogen concentrates to the methane adsorption capacities are calculated from the yields of kerogen concentrates from shales using equation (7), and these are expressed as a percentage using equation (8).

$$Q_{contribution} = Y_K \times Q_K \quad (7)$$

$$R_K = 100\% \times (Q_{contribution}/Q_{SH}) \quad (8)$$

Where, $Q_{contribution}$ is the quantity of methane adsorbed by the kerogen concentrates per gram shale; Y_K is the yield of kerogen concentrate; Q_K is the methane adsorption quantity of the kerogen concentrate; R_K is the percentage that the kerogen concentrate contributes to the methane adsorption in shale; Q_{SH} is the methane adsorption quantity of shale.

As expected, Table 2 indicates that kerogen concentrates have greater methane adsorption capacities than shales, both under dry and wet conditions. For the dry samples, the equilibrium adsorbed methane quantity for K1 is 22.2 mg/g, which is about 8 times higher than that for the SH1 (2.7 mg/g). The equilibrium adsorbed methane quantity of K2 (12.5 mg/g) is more than 6 times higher than that of SH2 (2.0 mg/g). K1 and K2 account for 97 and 68% of the equilibrium methane uptakes for the dry shales, respectively. The high content of clay minerals in SH2 could account for kerogen concentrates (K2) contributing less on methane adsorption under dry conditions. These contributions are higher than those of about

50% reported in other studies (Fan et al., 2014; Rexer et al., 2014) probably because the kerogens in this research are from overmatured shales, which are likely to contain more pores for methane adsorption.

Table 2. Methane adsorption capacities of the kerogen concentrates and shales, and the contributions made by kerogen concentrates to the capacities of the shales.

	Dry sample 1				Dry sample 2			
Pressure (bar)	Q_{K1} (mg/g)	Q_{SH1} (mg/g)	K1-$Q_{contribution}$ (mg/g)	R_{K1} (%)	Q_{K2} (mg/g)	Q_{SH2} (mg/g)	K2-$Q_{contribution}$ (mg/g)	R_{K2} (%)
5	4.0±0.1	0.9±0.1	0.5±0.1	53±1	2.1±0.1	0.5±0.1	0.2±0.1	45±1
50	11.5±0.3	2.1±0.1	1.4±0.1	66±4	6.3±0.3	1.4±0.1	0.7±0.1	50±4
100	15.4±1.2	2.3±0.2	1.9±0.1	79±10	8.7±0.9	1.6±0.1	1.0±0.1	58±7
150	16.6±1.4	2.5±0.2	2.0±0.2	81±10	9.3±0.9	1.7±0.1	1.0±0.1	59±7
300	18.9±1.6	2.6±0.2	2.3±0.2	88±11	10.6±1.0	1.9±0.2	1.2±0.1	63±8
Qm	22.2±1.8	2.7±0.3	2.7±0.2	97±12	12.5±1.2	2.0±0.2	1.4±0.1	68±9
	Wet sample 1				Wet sample 2			
Pressure (bar)	Q_{K1} (mg/g)	Q_{SH1} (mg/g)	K1-$Q_{contribution}$ (mg/g)	R_{K1} (%)	Q_{K2} (mg/g)	Q_{SH2} (mg/g)	K2-$Q_{contribution}$ (mg/g)	R_{K2} (%)
5	0.6±0.2	0.1±0.1	0.08±0.02	86±24	0.3±0.1	0.03±0.01	0.03±0.01	99±11
50	3.2±0.9	0.6±0.2	0.39±0.10	63±23	1.8±0.2	0.33±0.04	0.19±0.02	61±9
100	4.2±1.1	0.9±0.2	0.50±0.13	56±20	2.8±0.4	0.40±0.07	0.31±0.05	76±18
150	4.7±1.2	1.0±0.3	0.57±0.15	57±21	3.3±0.5	0.53±0.13	0.36±0.06	69±20
300	5.4±1.4	1.2±0.3	0.65±0.17	54±20	4.2±0.7	0.69±0.17	0.46±0.07	67±19
Qm	6.2±1.6	1.5±0.4	0.75±0.19	50±18	5.8±0.9	0.98±0.24	0.63±0.10	64±18

Q is the absolute methane quantity adsorbed by kerogen concentrate and shale from HPVA result, Q (<105 bar) is the absolute methane quantity convert from excess methane quantity by equation (3), Q (>105 bar) is the absolute methane quantity obtained from dual-site Langmuir model, $Q_{contribution}$ is the methane amount adsorbed by kerogen per gram of shale, calculated based on equation (7). R is the percentage kerogen concentrate contribution to the methane adsorption capacity of the shale calculated by equation (8). Q after pressure 105 bar is predicted by the Dual-site Langmuir model. Q_m is the predicted maximum methane amount adsorbed (monolayer capacity) when the isotherm reach equilibrium. The data points are the mean from triplicate experiments and the errors represent the dispersion of a dataset relative to its mean.

Due to the different isotherm profiles, at low pressure (5 bar), the dry kerogen concentrates nominally account for much less of the methane adsorption for the dry shales, 53 and 45% for SH1 and SH2, respectively. The ratio of the kerogen concentrate contribution increases with pressure. Most of methane adsorption of the dry shales takes place at a relatively low-pressure range due to the higher proportion of small micropores (Table 2). Moreover, dry kerogens, as discussed earlier (section 4.3.1), with larger micropores and small mesopores could have higher methane adsorption capacities than the organic matter in shales.

For the wet samples, the methane adsorption capacities of the kerogen concentrates are about 4-6 times higher than corresponding shales. K1 and K2 account for 50 and 64% respectively, of the methane adsorbed in the wet shales, which are less than the corresponding dry contributions. This could be due to the methane adsorption capacity of the isolated kerogen concentrates are reduced more by water than those of the organic matter within the shales. The data suggest that some organic matter within shales is 'shielded' from water as most organic matter in shale are surrounded by less porous minerals (section 4.2, Figure 2 FE-SEM), and methane can still adsorb on the unwet organic matter surface. Whereas water can wet most of organic matter in the isolated kerogen concentrate, having a strongly negative impact on their adsorption capacity. Moreover, in contrast to the dry samples, the apparent contributions of the kerogen concentrates to the methane adsorption capacities of the shales decrease with increasing pressure. Although moisture reduces the accessible micropores for methane adsorption for both shales and kerogen concentrates and results in shallower isotherms (Figure 3), the micropores in kerogen concentrates dominate methane adsorption in wet shales at low pressure (5 bar) with contribution ratios for K1 and K2 are 86 and 99% respectively, indicating minimal adsorption on minerals (Li et al., 2016; Li et al., 2019).

4.4 Pore characterization of the shales and kerogen concentrates

4.4.1 Moisture impact on low-pressure gas sorption isotherms The low-pressure gas isotherms of the dry (N_2, CO_2) and wet (N_2) kerogen concentrates and shales are compared in Figure 4 and 5. The CO_2 adsorption isotherms (Figure 5) are type I(b) and the N_2 sorption isotherms are type IV(a) with a hysteresis loop (Figure 4), a steeper gas uptake at low relative pressure arises from a higher proportion narrow micropores (Thommes et al., 2015). This confirms that the shales and kerogen concentrates contain mesopores and macropores, with the N_2 isotherms showing adsorption at a low relative pressure ($P/P°<0.1$) from micropores. The CO_2 isotherms show adsorption solely associated with micropores for both the shales and kerogen concentrates.

The quantity of adsorbed N_2 and shape of the hysteresis patterns of the dry and wet shales and kerogen concentrates are slightly different. For the dry shales (Figure 4A), the hysteresis loop is similar to hysteresis type H2 based on the classification of the hysteresis (Sing, 1985) which suggests the pores are very complex, with pore shapes including ink-bottle pores comprising necks and windows, inhomogeneous cylinder, slit and sphere pores, and other irregular pores (Sing, 1985; Thommes et al., 2015). The obvious desorption plateau in H2 hysteresis means there is pore-blocking or shielding from a narrow range of pore necks/windows, as cavitation occurs between 0.4-0.5 P/P°, indicating these necks and windows are all approximately <4 nm. This phenomenon still exists for wet shales (Figure 4B) having same isotherm and hysteresis types, but at a reduced pore volume or quantity of adsorbed N_2, indicating water is blocking a large majority of the pore and neck/window volume. The low-pressure hysteresis below 0.42 P/P° could be associated with the swelling of clay minerals (Bertier et al., 2016), which could affect the desorption in this pressure range.

For the dry kerogen concentrates (Figure 4C), the hysteresis loop is very similar to type H3 (Sing, 1985; Thommes et al., 2015), and the adsorption of N_2 increase rapidly at low relative pressure range (<0.1 P/P°), this indicates most of the pores are micro and mesopores with slit shape pore geometry. Pore necks/windows exist in kerogen concentrates with a large pore width ranging between 4-100 nm, as desorption isotherms decrease gradually, with the addition of necks/windows pores <4 nm (cavitation). However, most of these neck and window pores are blocked or filled when kerogen concentrates are equilibrated with moisture at 95% R.H. reducing interconnectivity (shown in Figure 4D, with little or no hysteresis for K1

and K2), and reducing N_2 adsorption. Another key difference between isotherms of kerogen concentrates and shales is that shales show greater hysteresis than kerogen concentrates, both wet and dry, which suggests that the hysteresis (narrow pore necks/windows) are mostly attributed by minerals or interfaces between minerals and kerogen.

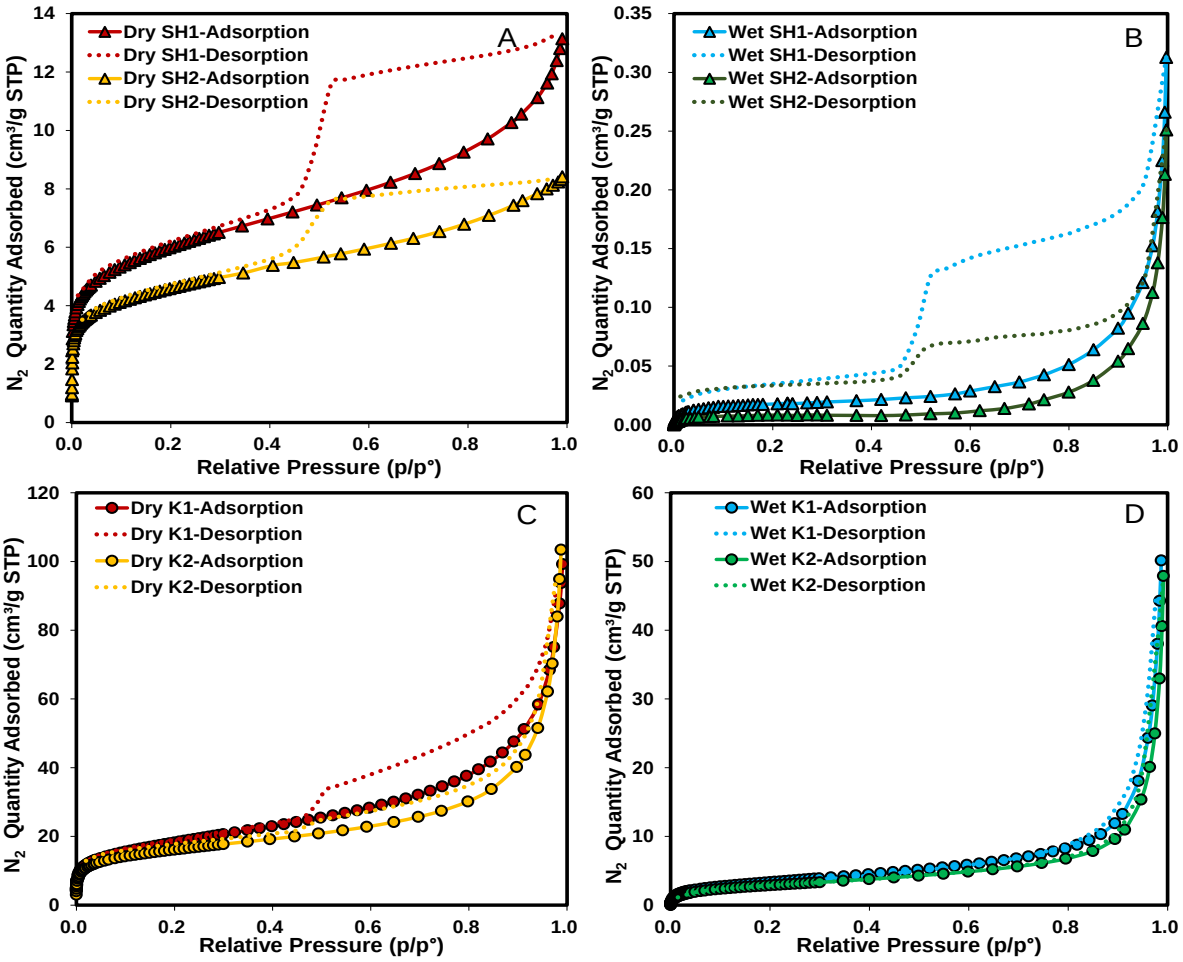

Figure 4. A comparison of low-pressure N_2 sorption isotherms of shales and kerogen concentrates under wet and dry conditions. A) N_2 isotherms of dry shales, B) N_2 isotherms of wet shales, C) N_2 isotherms of dry kerogen concentrates, D) N_2 isotherms of wet kerogen concentrates. P/P°, relative pressure, P is the absolute equilibrium pressure and P° is the saturation pressure of N_2 at -196 °C, 1 bar.

As expected, the extents of N_2 and CO_2 adsorption are much greater for the kerogen concentrates than the corresponding shales. Table 3 indicates that the maximum amounts of adsorbed N_2 for the dry kerogen concentrates are 99.2 and 103.4 cm^3/g which are 7-12 times higher than the corresponding dry shales (13.3 and 8.4 cm^3/g, respectively). SH1 and K1 have the higher SA and pore volume than SH2 and K2 as they have the higher TOC (Table 1). Similar

differences are observed for CO_2 adsorption (Figure 5), the maximum adsorbed CO_2 quantities are 10.9 and 8.9 cm^3/g on the two dry kerogen concentrates, which are about 4-5 times higher than the dry shales (2.4 and 1.7 cm^3/g) (Table 3). The BET SAs estimated from the N_2 isotherms are quite close to those from the CO_2 isotherms of the dry samples (Table 3), indicating the N_2 penetrates all the micropores that CO_2 can. Figure 5 indicates for the dry kerogens that K1 contains a greater micropore surface area (Table 3) and a greater proportion of smaller micropores than K2, consistent with the steeper methane adsorption isotherms (Figure 3).

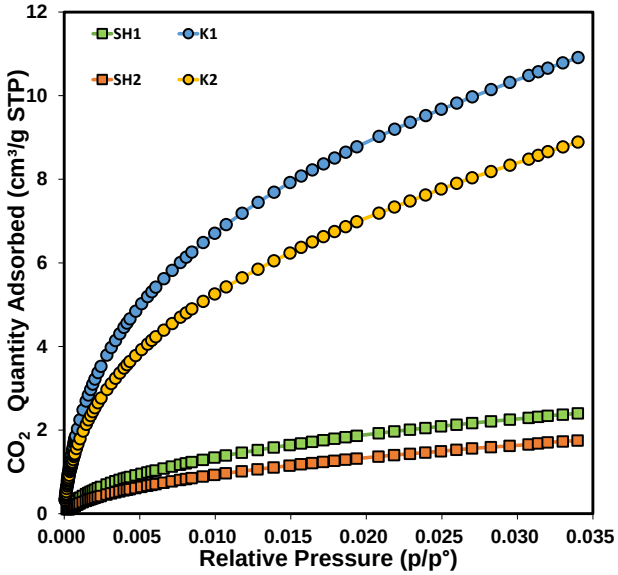

Figure 5. Comparison of low-pressure CO_2 adsorption isotherms of dry kerogen concentrates and shales at 0 °C. P/P°, relative pressure, P is the absolute equilibrium pressure and P° is the saturation pressure of CO_2 at 0 °C, 34.9 bar.

4.4.2 Moisture impact on pore characteristics The SAs of dry samples obtained from N_2 and CO_2 show little difference suggesting N_2 can penetrate all ultra-micropores of both wet and dry samples. Table 3 reveals that more than 81% of the BET SA for the kerogen concentrates is lost, at 95% R.H., K1 and K2, reducing from 65.7-58.8 m^2/g to 12.4-10.8 m^2/g, and 48-59% total pore volume is lost, reducing from 0.14-0.15 cm^3/g to 0.073-0.062 cm^3/g. The impact of moisture on the shales is even greater, with over 99% reduction in BET SA for SH1 and SH2, reducing from 21.7-16.7 m^2/g to 0.075-0.029 m^2/g, respectively, accompanied by a 98% loss in total pore volume. The swelling of clay minerals in wet shale might also result in the loss of pore volume (Feng et al., 2018; Bertier et al., 2016; Zhu and Xia, 2013).

Table 3. Maximum adsorbed gas quantities, surface areas and pore volumes of the shales and kerogen concentrates.

Sample	N_2 $Q_{Adsorbed}$ (cm^3/g)	CO_2 $Q_{Adsorbed}$ (cm^3/g)	SA_{BET} (m^2/g)	CO_2 SA_{BET} (m^2/g)	V_{micro} (cm^3/g)	V_{meso} (cm^3/g)	V_{macro} (cm^3/g)	V_{total} (cm^3/g)
Dry K1	99.2	10.9	65.7	68.0	0.0141	0.110	0.018	0.14
Dry K2	103.4	8.9	58.8	57.9	0.0140	0.114	0.023	0.15
Wet K1	50.1	/	12.4	/	0.0010	0.058	0.014	0.073
Wet K2	47.9	/	10.8	/	0.0011	0.044	0.017	0.062
Reduction K1 (%)	49	/	81	/	93	47	20	48
Reduction K2 (%)	54	/	82	/	92	62	24	59
Dry SH1	13.1	2.4	21.7	16.1	0.0069	0.012	0.00075	0.019
Dry SH2	8.4	1.7	16.7	12.6	0.0054	0.0067	0.00016	0.012
Wet SH1	0.31	/	0.075	/	0.0000039	0.00028	0.000063	0.00034
Wet SH2	0.25	/	0.029	/	0	0.00021	0.000056	0.00027
Reduction SH1 (%)	98	/	99.7	/	99.9	98	92	98
Reduction SH2 (%)	97	/	99.8	/	100	97	66	98

N_2 $Q_{Adsorbed}$ is the maximum adsorbed at 0.995 P/P°; CO_2 $Q_{Adsorbed}$ is the maximum adsorbed at 3.5×10^{-2} P/P°; SA_{BET} and CO_2 SA_{BET} are the surface areas calculated by BET theory; V_{micro}, V_{meso}, V_{macro} and V_{total} are the micropores, mesopore, macropore and the total pore volume (up to 100 nm) calculated by the NLDFT model.

Moisture also changes the PSD for the kerogen concentrates and shales. For the dry samples, the cumulative SA rises rapidly in the micropore range (Figure 6A, 6C). The two main peaks in incremental SA occur at 0.3-0.5 nm and 1-2 nm, with small peaks occurring at 2-10 nm (Figure 6B, 6D), confirming micropores contribute most of the SA, with some contributions from small

mesopores (less than 10 nm). Whereas for the wet kerogen concentrates and shales, micropores only make a small contribution to SA (Figure 6E, 6G). Although one of the main peaks in incremental SA occurs at 1.3-2 nm, most of the other peaks occur in the range of 2-50 nm, with no obvious differences evident (Figure 6F, 6H). Micropores less than 1.3 nm provide virtually no SA, making mesopores dominant for the wet samples (Figure 6F, 6H), suggesting pores less than 1.3 nm are either blocked or filled with water. Micropores contribute 9 and 10% for K1 and K2 and 36 and 44% for SH1 and SH2, respectively, of the dry pore volume (Figure 7A, 7C), since most of the maxima in the incremental pore volume occur in the mesopore range of 2-50 nm for both dry kerogen concentrates and shales. Whereas only a few maxima exist below 2 nm for the kerogen concentrates (Figure 7B), these maxima are relatively larger for the shales, indicating higher proportions of micropore volume, consistent with their steeper methane adsorption isotherms (Figure 3). However, micropores contribute less than 2% for the wet samples, with no pore volume below 1.3 nm (Figure 7E, 7G), indicating most micropores especially those less than 1.3 nm are blocked by water.

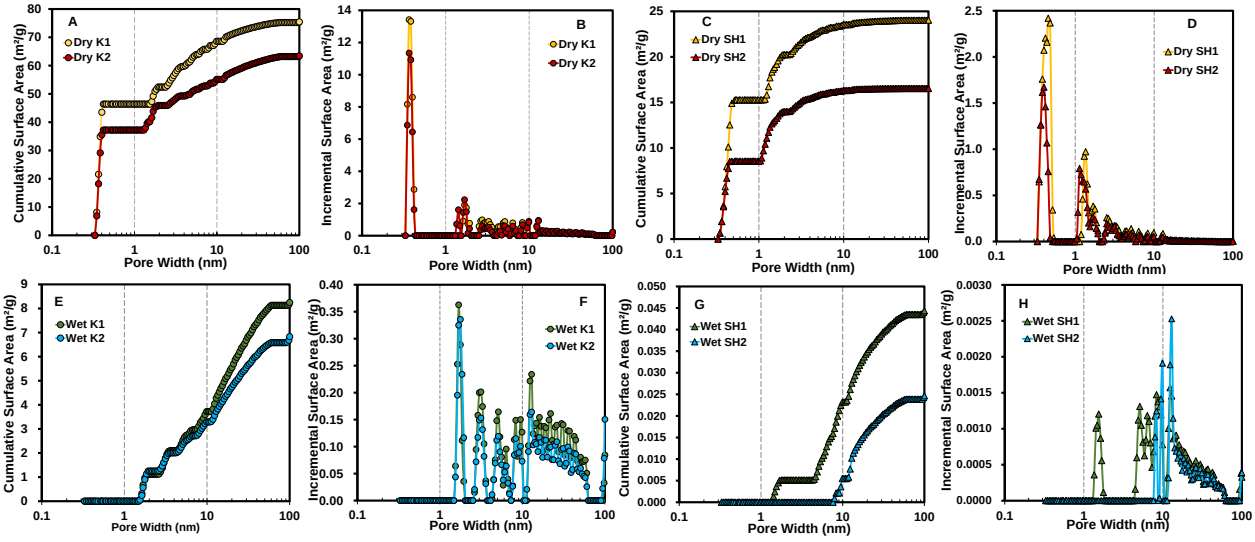

Figure 6. PSD and SA of dry (by N_2 and CO_2) and wet (by N_2) kerogen concentrates and shales. A) Cumulative SA and the pore width of dry kerogen concentrates, B) Incremental SA and pore width of dry kerogen concentrates, C) Cumulative SA and the pore width of dry shales, D) Incremental SA and pore width of dry shales, E) Cumulative SA and the pore width of wet kerogen concentrates, F) Incremental SA and pore width of wet kerogen concentrates, G) Cumulative SA and the pore width of wet shales, H) Incremental SA and pore width of wet shales.

Although mesopores contribute more than 55% of the total pore volume for both the dry or wet samples, the dry kerogen concentrates and shales have larger proportions of small mesopores (< 10 nm) volume (Figure 7B, 7D) than their wet counterparts (Figure 7F, 7H), since most higher peaks of incremental pore volume only exist between 10-50 nm under wet conditions, reducing the small mesopores (<10 nm) contribution (Figure 7F, 7H). This suggests water blocking micropores can also reduce the interconnectivity to larger pores reducing the pore volume in meso and even macropores, but by a lesser and different extent (Table 3).

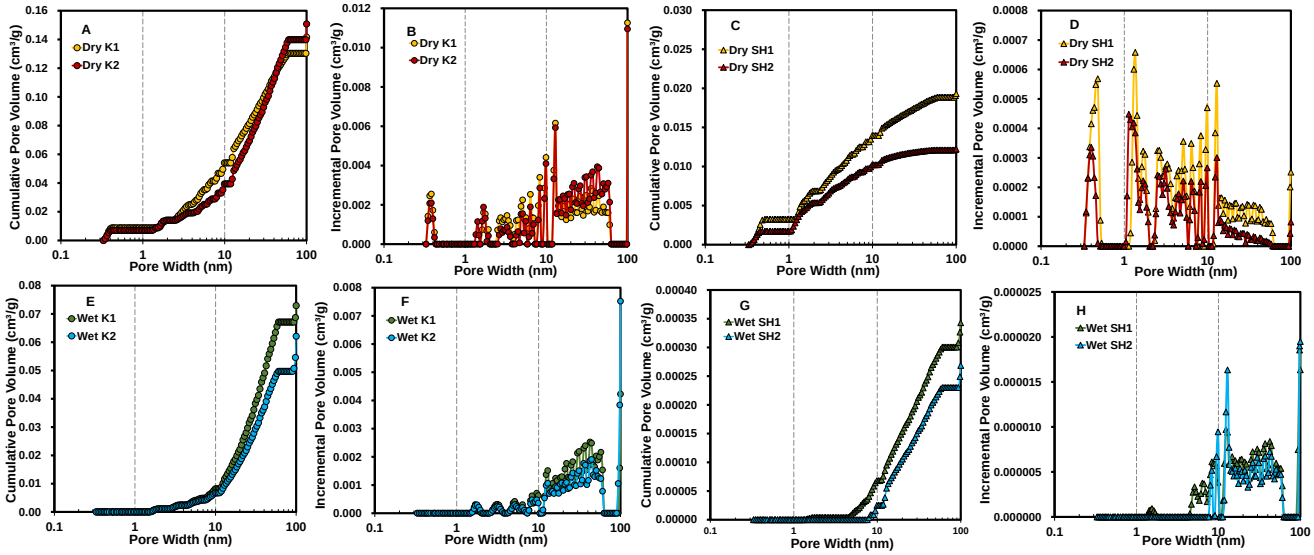

Figure 7. PSD and pore volume of dry (by N_2 and CO_2) and wet (by N_2) kerogen concentrates and shales. A) Cumulative pore volume and the pore width of dry kerogen concentrates, B) Incremental pore volume and pore width of dry kerogen concentrates, C) Cumulative pore volume and the pore width of dry shales, D) Incremental pore volume and pore width of dry shales, E) Cumulative pore volume and the pore width of wet kerogen concentrates, F) Incremental pore volume and pore width of wet kerogen concentrates, G) Cumulative pore volume and the pore width of wet shales, H) Incremental pore volume and pore width of wet shales.

Table 3 confirms that moisture has the greatest impact on micropores, followed by mesopores and macropores in both kerogen concentrates (93-92, 47-62 and 20-24% reductions for micropore, mesopore, and macropore volumes, respectively) and shales (99.9-100, 98-97 and 92-66%, respectively), which makes the extent of reduction for SA larger than that for pore volume since most of the SA is provided by micropores, whereas most of the pore volume is provided by mesopores. Also, Table 3 indicates that the reduction in SA and

pore volume for the shales are much higher than for the kerogen concentrates. This is because the proportion of micropores in shale (36-44%) is much higher than for kerogen (9-10%). In addition, the large amount of clay minerals in some shales are responsible for these shales being most easily affected by water (Feng et al., 2018; Bertier et al., 2016; Ismadji et al., 2015; Kuila et al., 2014; Liming et al., 2012b; Zhu and Xia, 2013).

Water molecules hinder access to the smaller micropores, as shown in Figure 6 and 7, for a cylindrical/slit pore with a diameter of equal to or less than 1.3 nm. Less water is adsorbed in the larger micropores (together with mesopores) due to the reducing energy potential for adsorption (Dubinin, 1966; Gregg and Sing, 1982; Ruthven, 1984). Also, water is adsorbed in micropores first when these can be accessed. For the pores larger than 1.3 nm, water occupies some adsorption sites and can form a cluster of molecules leading to a film (or condensate) which reduces both the accessible pore volume and SA, while other gases can still gain access if the pores are not totally blocked. It is believed that thicker water films can reduce pore volume more (Li et al., 2016). The low-pressure adsorption isotherm results have indicated that the micropores, mesopores and macropores are largely connected by narrow pore necks building a complex pore system. The water volume uptake calculated by equation (2) indicates that 33 and 40% of the pore volume for SH1 and SH2 are occupied by water, whereas more than 98% accessible pore volume of shales are reduced after sample become wet, suggesting the water reduce the pore volume by taking up the pore volume as well as by blocking the micropore pore necks connecting to larger pores. The size of the pore neck matters, when the pore necks are less than 1.3 nm, water molecule clusters can block the necks preventing other gases being transported into larger pores, but when the pore neck is larger, there is still enough space for the other gas to go into the bigger pores.

4.5 Depiction of the impact of moisture on methane adsorption capacity

Figure 8 illustrates how moisture can reduce the methane adsorption capacity for kerogens by 1) occupying adsorption surfaces. Water, as the polar molecule gives stronger interactions with the same adsorption surface (non-polar or polar) than the non-polar methane molecules, can occupy adsorption sites (Chalmers and Bustin, 2010; Chalmers and Bustin, 2007; Huang et al., 2018; Zhao et al., 2018); 2) blocking micropore access and filing mesopores. As for the mesopores connecting with different size of pore necks (smaller than 1.3 nm and larger than 1.3 nm) methane can occupy most of the sorption surface in the dry samples (Figure 8A).

However, after samples become wet, much of the available sorption surface is taken up by water, or most pores with narrow pore necks become inaccessible since water blocks access to micropore less than 1.3 nm (Figure 8B).

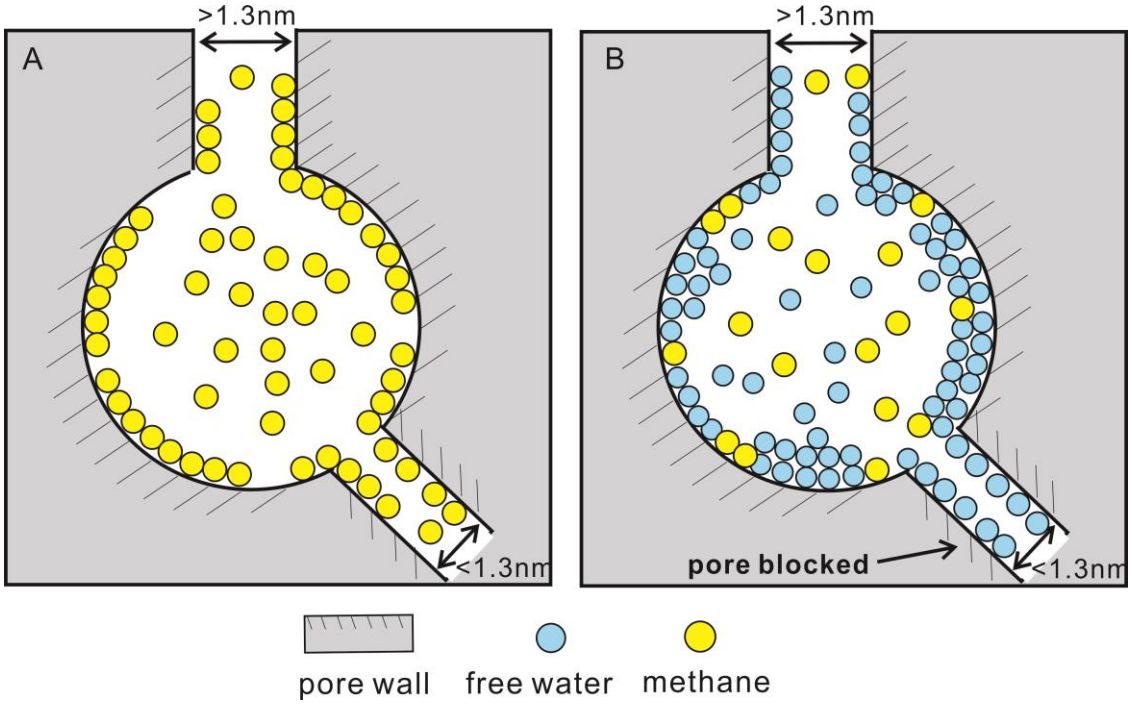

Figure 8. Depiction of the impact of moisture on methane adsorption in small mesopore and connecting micropores for kerogens. A) Methane adsorption in dry samples, B) Methane adsorption in wet samples, with water blocking micropore access and filling mesopores.

Moisture can affect methane adsorption differently for kerogen concentrates and shales. According to methane adsorption results, the reduction of K1 (72%) is higher than K2 (54%) since K1 has more narrow pore necks as more evident cavitation occurs in the desorption isotherms (Figure 4C), and most pore necks are blocked after moisture equilibrated (Figure 4D with little or no hysteresis). However, for shales, the reductions (46-51%) are comparable as they have similar pore networks (Figure 4A). Furthermore, the reductions in SA and pore volume measured are higher than those for the equilibrium methane adsorption capacities. This can be explained by ice having a greater effect on blocking access to pores than water. It is because the SA and pore volume are measured at sorption experiment temperature of -196 °C for low-pressure N_2, bulk pore water or water clusters will exist as ice crystals (Pauling, 1935), with a lattice of 0.45 nm width and 0.73 nm height (Bragg, 1921), which could occupy more space so reducing pore SA and volume to a greater extent. Whereas water molecules

564 are depicted with a diameter of 0.28 nm (D'Arrigo, 1978; Zhang and Xu, 1995) in the methane
565 adsorption experiment temperature (25 °C). Furthermore, the pore blocking threshold of 1.3
566 nm occurs with ice crystals but not necessarily water meaning the blocking effects are
567 probably slightly exaggerated at -196 °C.

568 **5. Implication for GIP**

569 The classical GIP based on the shale gas holding capacity is estimated from the total amount
570 of free gas and adsorbed gas content by equation (9) (Tang et al., 2016). However, most GIP
571 estimations use dry samples without considering the effect of moisture, and therefore could
572 be overestimated. This research provides a realistic method for the measurement of the
573 accessible pore volume of moisture equilibrated shales and reveal the moisture impact on the
574 adsorbed gas content, making a more accurate GIP estimation of wet shales possible. The
575 GIPs (the shale gas holding capacity) of dry and wet shales are listed in Table 4 which are
576 calculated by equation (9), the dry porosity is obtained from MIP and wet porosity is
577 calculated based on equation (10).

578 $$GIP = n_{free} + n_a = n_{free} + n_e + V_a \times \rho_g = V_{tot} \times \rho_g + n_e \quad (9)$$

579 $$Porosity_{wet} = \frac{V_{wet\ pore}}{V_{sh}} = 1 - \frac{\rho_{wet\ bulk}}{\rho_{wet\ sk}} = 1 - \frac{\rho_{dry\ bulk}}{\rho_{wet\ sk}} \times (1 + W) \quad (10)$$

580 where, n_{free} is the free gas in the pore; n_a is the absolute adsorption quantity; n_e is the
581 excess adsorption quantity; V_a is the pore volume for gas to adsorb into; ρ_g is the density of
582 the bulk gas; V_{tot} is the total pore volume accessible to gas in shale; $Porosity_{wet}$ is the
583 porosity of wet shale; $V_{wet\ pore}$ is the pore volume of wet shale; V_{sh} is the shale sample
584 volume.

585 Table 4. The porosity, total pore volume and the estimated GIP of shales.

Sample	Porosity (%)	V_{tot} (m^3/t)	n_a (kg/t)	n_{free} (kg/t)	GIP (kg/t)
Dry SH1	10.2	0.043	1.5	10.4	11.9
Dry SH2	4.0	0.016	1.1	3.7	4.8
Wet SH1	6.8	0.028	0.73	6.9	7.6
Wet SH2	2.4	0.009	0.44	2.2	2.7

586

Pressure and temperature effects on the free and adsorbed gas content cannot be neglected (Chen et al., 2018; Luffel and Guidry, 1992; Ross and Bustin, 2007; Tang et al., 2016). It is estimated that the actual shale reservoir pressure and temperature of Longmaxi shale, Sichuan Basin with a depth of 4000 m are about 600 bar and more than 100 °C (Li et al., 2018; Tang et al., 2016). An average reduction of 45% for adsorbed gas content from 25 °C to 100 °C is applied based on the literature (Ji et al., 2015; Rexer et al., 2013; Whitelaw et al., 2019; Zou et al., 2017). The total accessible pore volume (V_{tot}) of shale is calculated from the porosity, the density of methane at 600 bar and 100 °C is 241.03 kg/m^3 obtained from REFPROP version 8.0 software and the excess adsorption quantity (equation (3)) is from the methane adsorption experiments. The estimated GIP of the shales at 600 bar and 100 °C are listed in Table 4, and the dominant gas is free gas for both dry and wet shales. The calculated GIP of the dry shales, SH1 and SH2 (maximum GIP) are 11.9 and 4.8 kg/t, respectively, similar to the range of 3.2-6.4 kg/t for Longmaxi shale (Tang et al., 2016). The GIP of the wet shales SH1 and SH2 (minimum GIP) are 7.6 and 2.7 kg/t, respectively, indicating that the estimated GIP can reduce by up to 36-45% when moisture is considered.

6. Conclusions

This is the first time that the impact of moisture on PSD and methane adsorption capacities of kerogens and shales have been compared and the following conclusions can be drawn.

(1) Moisture has a detrimental effect on methane adsorption capacity, reductions for the kerogen concentrates and shales being 54-72% and 46-51%, respectively, at 95% R.H.. The kerogen concentrates are the most important matter in shale for methane adsorption, which account for most (97 and 68% for dry SH1 and SH2, 50 and 64% for wet SH1 and SH2) of the equilibrium methane adsorption capacities of the shales within experimental error.

(2) At lower pressures, dry shales display a steeper rise of methane adsorption than dry kerogen concentrates suggesting that demineralisation could access larger micropores and smaller mesopores. The less steep isotherms of wet samples suggest they require higher pressure and pore energy to adsorb same amount of gas as the dry samples.

(3) The kerogen concentrates have much higher average SA (62.2 m^2/g compared to 19.2 m^2/g) and average pore volume (0.15 cm^3/g compared to 0.016 cm^3/g) than corresponding shales. Moisture significantly reduces the SA (81% for kerogen, and 99%

for shale) and total pore volume for kerogens concentrates (48-49%) and shales (98%), by filling or blocking micropores less than 1.3 nm, obstructing pore necks connecting to micropores and mesopores stopping gas transport, occupying adsorption sites, or swelling clays (in shale) to reduce accessible pores. These reductions are much larger than reductions observed for methane adsorption as ice in the N_2 low-pressure measurements reducing access to pores much more than liquid water for methane adsorption.

(4) This research provides a realistic method for accurate GIP estimation of moisture equilibrated shales. The calculated GIP of the dry SH1 and SH2 (maximum GIP) are 11.9 and 4.8 kg/t, and the GIP of the wet shales (minimum GIP) 7.6 and 2.7 kg/t, indicating the GIP reduces by 36-45% when moisture is considered for the shales investigated.

Acknowledgments

The authors greatly acknowledge financial support by the National Environment Research Council (Grant no: NE/C507002/1) and the Faculty of Engineering Research Excellence PhD Scholarship for Wei Li provided by the University of Nottingham. The British Geological Survey is acknowledged for experimental support.

References

Abràmoff, M.D., Magalhães, P.J., Ram, S.J., 2004. Image processing with ImageJ. Biophotonics international 11, 36-42.

Adesida, A.G., Akkutlu, I., Resasco, D.E., Rai, C.S., 2011. Characterization of barnett shale kerogen pore size distribution using DFT analysis and grand canonical monte carlo simulations, SPE annual technical conference and exhibition. Society of Petroleum Engineers.

Bertier, P., Schweinar, K., Stanjek, H., Ghanizadeh, A., Clarkson, C.R., Busch, A., Kampman, N., Prinz, D., Amann-Hildenbrand, A., Krooss, B.M., 2016. On the use and abuse of N2 physisorption for the characterization of the pore structure of shales, The clay minerals society workshop lectures series, pp. 151-161.

Bragg, W., 1921. The crystal structure of ice. Proceedings of the Physical Society of London 34, 98.

Brunauer, S., Emmett, P.H., Teller, E., 1938. Adsorption of gases in multimolecular layers. Journal of the American chemical society 60, 309-319.

Cao, T., Song, Z., Wang, S., Xia, J., 2015. A comparative study of the specific surface area and pore structure of different shales and their kerogens. Science China Earth Sciences 58, 510-522.

Chalmers, G.R., Bustin, M.R., 2010. PS The Effects and Distribution of Moisture in Gas Shale Reservoir Systems. AAPG Annual Convention and Exhibition.

Chalmers, G.R., Bustin, R.M., 2007. The organic matter distribution and methane capacity of the Lower Cretaceous strata of Northeastern British Columbia, Canada. International Journal of Coal Geology 70, 223-239.
Chen, C., Hu, D., Westacott, D., Loveless, D., 2013. Nanometer-scale characterization of microscopic pores in shale kerogen by image analysis and pore-scale modeling. Geochemistry, Geophysics, Geosystems 14, 4066-4075.
Chen, M., Kang, Y., Zhang, T., Li, X., Wu, K., Chen, Z., 2018. Methane adsorption behavior on shale matrix at in-situ pressure and temperature conditions: Measurement and modeling. Fuel 228, 39-49.
Chen, Y., Jiang, S., Zhang, D., Liu, C., 2017. An adsorbed gas estimation model for shale gas reservoirs via statistical learning. Applied energy 197, 327-341.
Curtis, J.B., 2002. Fractured shale-gas systems. AAPG bulletin 86, 1921-1938.
Dai, J., Zou, C., Liao, S., Dong, D., Ni, Y., Huang, J., Wu, W., Gong, D., Huang, S., Hu, G., 2014. Geochemistry of the extremely high thermal maturity Longmaxi shale gas, southern Sichuan Basin. Organic Geochemistry 74, 3-12.
D'Arrigo, J.S., 1978. Screening of membrane surface charges by divalent cations: an atomic representation. American Journal of Physiology-Cell Physiology 235, C109-C117.
Day, S., Sakurovs, R., Weir, S., 2008. Supercritical gas sorption on moist coals. International Journal of Coal Geology 74, 203-214.
Dong, D., Shi, Z., Guan, Q., Jiang, S., Zhang, M., Zhang, C., Wang, S., Sun, S., Yu, R., Liu, D., 2018. Progress, challenges and prospects of shale gas exploration in the Wufeng–Longmaxi reservoirs in the Sichuan Basin. Natural Gas Industry B 5, 415-424.
Dongjun, F., Zongquan, H., Bo, G., Yongmin, P., Wei, D., 2016. Analysis of shale gas reservoir—forming condition of Wufeng Formation—Longmaxi Formation in Southeast Sichuan Basin. Geological Review 62, 1521-1532.
Dubinin, M., 1966. Chemistry and physics of carbon. M. Dekker, New York, 51-120.
Durand, B., 1980. Kerogen: Insoluble organic matter from sedimentary rocks. Editions technip.
Fan, E., Tang, S., Zhang, C., Guo, Q., Sun, C., 2014. Methane sorption capacity of organics and clays in high-over matured shale-gas systems. Energy Exploration and Exploitation 32, 927-942.
Feng, D., Li, X., Wang, X., Li, J., Sun, F., Sun, Z., Zhang, T., Li, P., Chen, Y., Zhang, X., 2018. Water adsorption and its impact on the pore structure characteristics of shale clay. Applied Clay Science 155, 126-138.
Gasparik, M., Bertier, P., Gensterblum, Y., Ghanizadeh, A., Krooss, B.M., Littke, R., 2014. Geological controls on the methane storage capacity in organic-rich shales. International Journal of Coal Geology 123, 34-51.
Gasparik, M., Ghanizadeh, A., Bertier, P., Gensterblum, Y., Bouw, S., Krooss, B.M., 2012. High-pressure methane sorption isotherms of black shales from the Netherlands. Energy & fuels 26, 4995-5004.
Gregg, S., Sing, K., 1982. W. Adsorption, surface area and porosity. London: Academic Press, 195-197.
Guthrie, J.M., Pratt, L.M., 1994. Geochemical indicators of depositional environment and source-rock potential for the Upper Ordovician Maquoketa Group, Illinois Basin. AAPG bulletin 78, 744-757.
Heller, R., Zoback, M., 2014. Adsorption of methane and carbon dioxide on gas shale and pure mineral samples. Journal of Unconventional Oil and Gas Resources 8, 14-24.

Hu, H., 2014. Methane adsorption comparison of different thermal maturity kerogens in shale gas system. Chinese Journal of Geochemistry 33, 425-430.
Huang, L., Ning, Z., Wang, Q., Zhang, W., Cheng, Z., Wu, X., Qin, H., 2018. Effect of organic type and moisture on CO 2/CH 4 competitive adsorption in kerogen with implications for CO 2 sequestration and enhanced CH 4 recovery. Applied Energy 210, 28-43.
Hunt, J., 1979. Petroleum geochemistry and geology, San Francisco, California.
Ismadji, S., Soetaredjo, F.E., Ayucitra, A., 2015. The Characterization of Clay Minerals and Adsorption Mechanism onto Clays, Clay Materials for Environmental Remediation. Springer, pp. 93-112.
Jarvie, D.M., Hill, R.J., Ruble, T.E., Pollastro, R.M., 2007. Unconventional shale-gas systems: The Mississippian Barnett Shale of north-central Texas as one model for thermogenic shale-gas assessment. AAPG bulletin 91, 475-499.
Ji, L., Zhang, T., Milliken, K.L., Qu, J., Zhang, X., 2012. Experimental investigation of main controls to methane adsorption in clay-rich rocks. Applied Geochemistry 27, 2533-2545.
Ji, W., Song, Y., Jiang, Z., Chen, L., Li, Z., Yang, X., Meng, M., 2015. Estimation of marine shale methane adsorption capacity based on experimental investigations of Lower Silurian Longmaxi formation in the Upper Yangtze Platform, south China. Marine and Petroleum Geology 68, 94-106.
Ji, W., Song, Y., Rui, Z., Meng, M., Huang, H., 2017. Pore characterization of isolated organic matter from high matured gas shale reservoir. International Journal of Coal Geology 174, 31-40.
Jin, Z., Firoozabadi, A., 2014. Effect of water on methane and carbon dioxide sorption in clay minerals by Monte Carlo simulations. Fluid Phase Equilibria 382, 10-20.
Joubert, J.I., Grein, C.T., Bienstock, D., 1973. Sorption of methane in moist coal. Fuel 52, 181-185.
Kuila, U., McCarty, D.K., Derkowski, A., Fischer, T.B., Topór, T., Prasad, M., 2014. Nano-scale texture and porosity of organic matter and clay minerals in organic-rich mudrocks. Fuel 135, 359-373.
Li, J., Li, X., Wang, X., Li, Y., Wu, K., Shi, J., Yang, L., Feng, D., Zhang, T., Yu, P., 2016. Water distribution characteristic and effect on methane adsorption capacity in shale clay. International Journal of Coal Geology 159, 135-154.
Li, J., Zhou, S., Gaus, G., Li, Y., Ma, Y., Chen, K., Zhang, Y., 2018. Characterization of methane adsorption on shale and isolated kerogen from the Sichuan Basin under pressure up to 60 MPa: Experimental results and geological implications. International Journal of Coal Geology 189, 83-93.
Li, W., Pang, X., Snape, C., Zhang, B., Zheng, D., Zhang, X., 2019. Molecular Simulation Study on Methane Adsorption Capacity and Mechanism in Clay Minerals: Effect of Clay Type, Pressure, and Water Saturation in Shales. Energy & Fuels 33, 765-778.
Liming, J., Junli, Q., Tongwei, Z., 2012a. Experiments on methane adsorption of common clay minerals in shale. Earth Science: Journal of China University of Geosciences 37, 1043-1050.
Liming, J., Junli, Q., Yanqing, X., Tongwei, Z., 2012b. Micro-pore characteristics and methane adsorption properties of common clay minerals by electron microscope scanning. Acta Petrolei Sinica 33, 249-256.
Liu, J., Sun, N., Sun, C., Liu, H., Snape, C., Li, K., Wei, W., Sun, Y., 2015. Spherical potassium intercalated activated carbon beads for pulverised fuel CO2 post-combustion capture. Carbon 94, 243-255.

746 Liu, K., Ostadhassan, M., Zou, J., Gentzis, T., Rezaee, R., Bubach, B., Carvajal-Ortiz, H., 2018.
747 Nanopore structures of isolated kerogen and bulk shale in Bakken Formation. Fuel 226, 441-
748 453.
749 Loucks, R.G., Reed, R.M., Ruppel, S.C., Hammes, U., 2012. Spectrum of pore types and
750 networks in mudrocks and a descriptive classification for matrix-related mudrock pores.
751 AAPG bulletin 96, 1071-1098.
752 Loucks, R.G., Reed, R.M., Ruppel, S.C., Jarvie, D.M., 2009. Morphology, genesis, and
753 distribution of nanometer-scale pores in siliceous mudstones of the Mississippian Barnett
754 Shale. Journal of sedimentary research 79, 848-861.
755 Luffel, D., Guidry, F., 1992. New core analysis methods for measuring reservoir rock
756 properties of Devonian shale. Journal of Petroleum Technology 44, 1,184-181,190.
757 Ma, L., Fauchille, A.-L., Dowey, P.J., Pilz, F.F., Courtois, L., Taylor, K.G., Lee, P.D., 2017.
758 Correlative multi-scale imaging of shales: a review and future perspectives. Geological
759 Society, London, Special Publications 454, 175-199.
760 Malik, S., Smith, L., Sharman, J., Holt, E.M., Rigby, S.P., 2016. Pore structural characterization
761 of fuel cell layers using integrated mercury porosimetry and computerized X-ray
762 tomography. Industrial & Engineering Chemistry Research 55, 10850-10859.
763 Merkel, A., Fink, R., Littke, R., 2016. High pressure methane sorption characteristics of
764 lacustrine shales from the Midland Valley Basin, Scotland. Fuel 182, 361-372.
765 Milliken, K.L., Rudnicki, M., Awwiller, D.N., Zhang, T., 2013. Organic matter–hosted pore
766 system, Marcellus formation (Devonian), Pennsylvania. AAPG bulletin 97, 177-200.
767 Pang, Y., Tian, Y., Soliman, M.Y., Shen, Y., 2019. Experimental measurement and analytical
768 estimation of methane absorption in shale kerogen. Fuel 240, 192-205.
769 Pauling, L., 1935. The structure and entropy of ice and of other crystals with some
770 randomness of atomic arrangement. Journal of the American Chemical Society 57, 2680-
771 2684.
772 Peng, J., Milliken, K., Fu, Q., Janson, X., Hamlin, S., 2020. Grain assemblages and diagenesis
773 in organic-rich mudrocks, Late Pennsylvanian Cline Shale (Wolfcamp D), Midland Basin,
774 Texas, 2019 AAPG Annual Convention and Exhibition.
775 Peng, J., Milliken, K.L., Fu, Q., 2019. Quartz types in the Upper Pennsylvanian organic-rich
776 Cline Shale (Wolfcamp D), Midland Basin, Texas: Implications for silica diagenesis, porosity
777 evolution and rock mechanical properties. Sedimentology.
778 Qi, L., Tang, X., Wang, Z., Peng, X., 2017. Pore characterization of different types of coal
779 from coal and gas outburst disaster sites using low temperature nitrogen adsorption
780 approach. International Journal of Mining Science and Technology 27, 371-377.
781 Rexer, T.F., Benham, M.J., Aplin, A.C., Thomas, K.M., 2013. Methane adsorption on shale
782 under simulated geological temperature and pressure conditions. Energy & Fuels 27, 3099-
783 3109.
784 Rexer, T.F., Mathia, E.J., Aplin, A.C., Thomas, K.M., 2014. High-pressure methane adsorption
785 and characterization of pores in Posidonia shales and isolated kerogens. Energy & Fuels 28,
786 2886-2901.
787 Ross, D.J., Bustin, R.M., 2007. Shale gas potential of the lower Jurassic Gordondale member,
788 northeastern British Columbia, Canada. Bulletin of Canadian Petroleum Geology 55, 51-75.
789 Ross, D.J., Bustin, R.M., 2008. Characterizing the shale gas resource potential of Devonian–
790 Mississippian strata in the Western Canada sedimentary basin: Application of an integrated
791 formation evaluation. AAPG bulletin 92, 87-125.

Ross, D.J., Bustin, R.M., 2009. The importance of shale composition and pore structure upon gas storage potential of shale gas reservoirs. Marine and petroleum Geology 26, 916-927.
Rouquerol, J., Llewellyn, P., Rouquerol, F., 2007. Is the BET equation applicable to microporous adsorbents. Stud. Surf. Sci. Catal 160, 49-56.
Ruthven, D.M., 1984. Principles of adsorption and adsorption processes. John Wiley & Sons.
Sing, K.S., 1985. Reporting physisorption data for gas/solid systems with special reference to the determination of surface area and porosity (Recommendations 1984). Pure and applied chemistry 57, 603-619.
Sircar, S., 1999. Gibbsian surface excess for gas adsorption revisited. Industrial & engineering chemistry research 38, 3670-3682.
Tang, L., Song, Y., Jiang, Z., Pang, X., Li, Z., Li, Q., Li, W., Tang, X., Pan, A., 2019. Influencing factors and mathematical prediction of shale adsorbed gas content in the Upper Triassic Yanchang Formation in the Ordos Basin, China. Minerals 9, 265.
Tang, X., Ripepi, N., Stadie, N.P., Yu, L., Hall, M.R., 2016. A dual-site Langmuir equation for accurate estimation of high pressure deep shale gas resources. Fuel 185, 10-17.
Thommes, M., Kaneko, K., Neimark, A.V., Olivier, J.P., Rodriguez-Reinoso, F., Rouquerol, J., Sing, K.S., 2015. Physisorption of gases, with special reference to the evaluation of surface area and pore size distribution (IUPAC Technical Report). Pure and Applied Chemistry 87, 1051-1069.
Wang, S., Javadpour, F., Feng, Q., 2016. Confinement correction to mercury intrusion capillary pressure of shale nanopores. Scientific reports 6, 20160.
Weniger, P., Franců, J., Hemza, P., Krooss, B.M., 2012. Investigations on the methane and carbon dioxide sorption capacity of coals from the SW Upper Silesian Coal Basin, Czech Republic. International Journal of Coal Geology 93, 23-39.
Whitelaw, P., Uguna, C.N., Stevens, L.A., Meredith, W., Snape, C.E., Vane, C.H., Moss-Hayes, V., Carr, A.D., 2019. Shale gas reserve evaluation by laboratory pyrolysis and gas holding capacity consistent with field data. Nature communications 10, 1-10.
Xiong, J., Liu, X., Liang, L., Zeng, Q., 2017. Adsorption of methane in organic-rich shale nanopores: An experimental and molecular simulation study. Fuel 200, 299-315.
Young, J.F., 1967. Humidity control in the laboratory using salt solutions—a review. Journal of Applied Chemistry 17, 241-245.
Zhang, T., Ellis, G.S., Ruppel, S.C., Milliken, K., Yang, R., 2012. Effect of organic-matter type and thermal maturity on methane adsorption in shale-gas systems. Organic geochemistry 47, 120-131.
Zhang, Y., Xu, Z., 1995. Atomic radii of noble gas elements in condensed phases. American Mineralogist 80, 670-675.
Zhao, T., Li, X., Ning, Z., Zhao, H., Li, M., 2018. Molecular simulation of methane adsorption on type II kerogen with the impact of water content. Journal of Petroleum Science and Engineering 161, 302-310.
Zhu, Y., Xia, X., 2013. Comparison and explanation of the absorptivity of organic matters and clay minerals in shales. Journal of China Coal Society 38, 812-816.
Zolfaghari, A., Dehghanpour, H., Holyk, J., 2017a. Water sorption behaviour of gas shales: I. Role of clays. International Journal of Coal Geology 179, 130-138.
Zolfaghari, A., Dehghanpour, H., Xu, M., 2017b. Water sorption behaviour of gas shales: II. Pore size distribution. International Journal of Coal Geology 179, 187-195.

837 Zou, C., Dong, D., Wang, S., Li, J., Li, X., Wang, Y., Li, D., Cheng, K., 2010. Geological
838 characteristics and resource potential of shale gas in China. Petroleum exploration and
839 development 37, 641-653.
840 Zou, J., Rezaee, R., Liu, K., 2017. Effect of temperature on methane adsorption in shale gas
841 reservoirs. Energy & Fuels 31, 12081-12092.
842 Zou, J., Rezaee, R., Xie, Q., You, L., Liu, K., Saeedi, A., 2018. Investigation of moisture effect
843 on methane adsorption capacity of shale samples. Fuel 232, 323-332.

844

Comparison of the Impact of Moisture on Methane Adsorption and Nanoporosity for Over Mature Shales and their Kerogens

Supplementary material

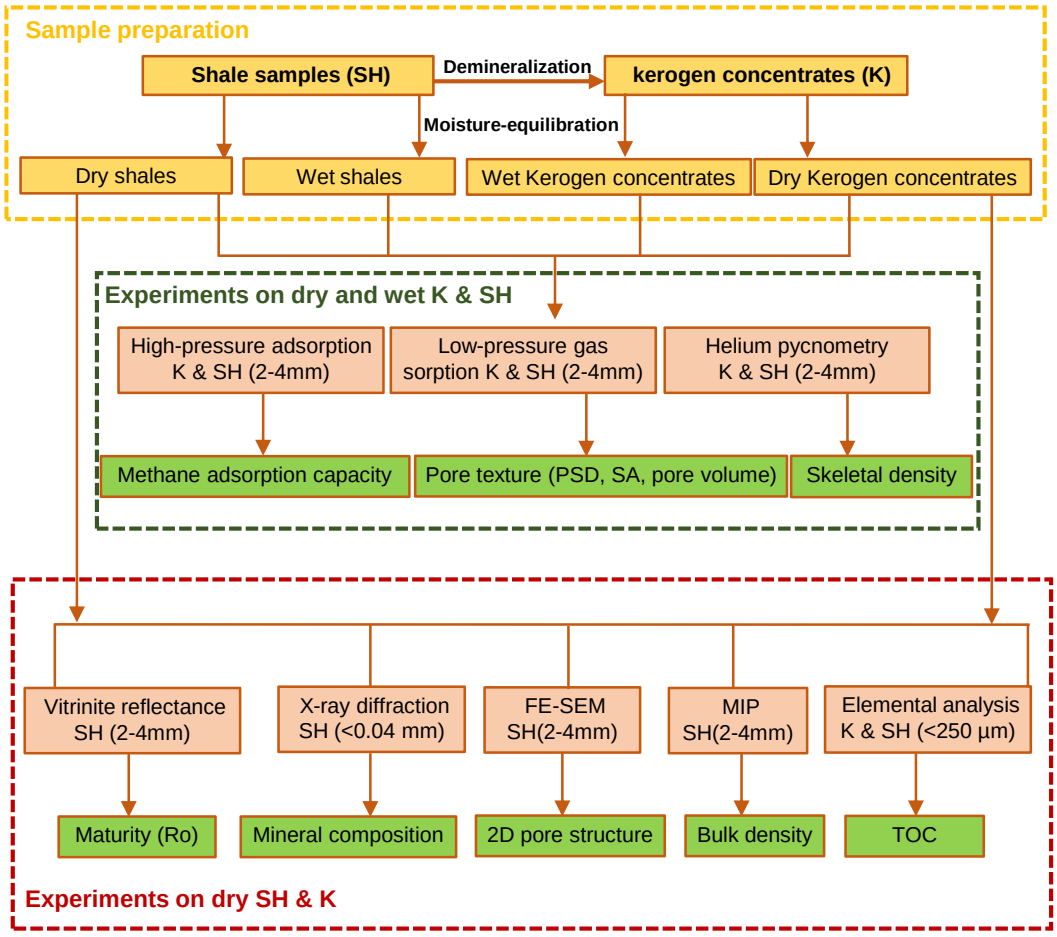

Figure 1S. The flowchart of sample preparations and experiments.

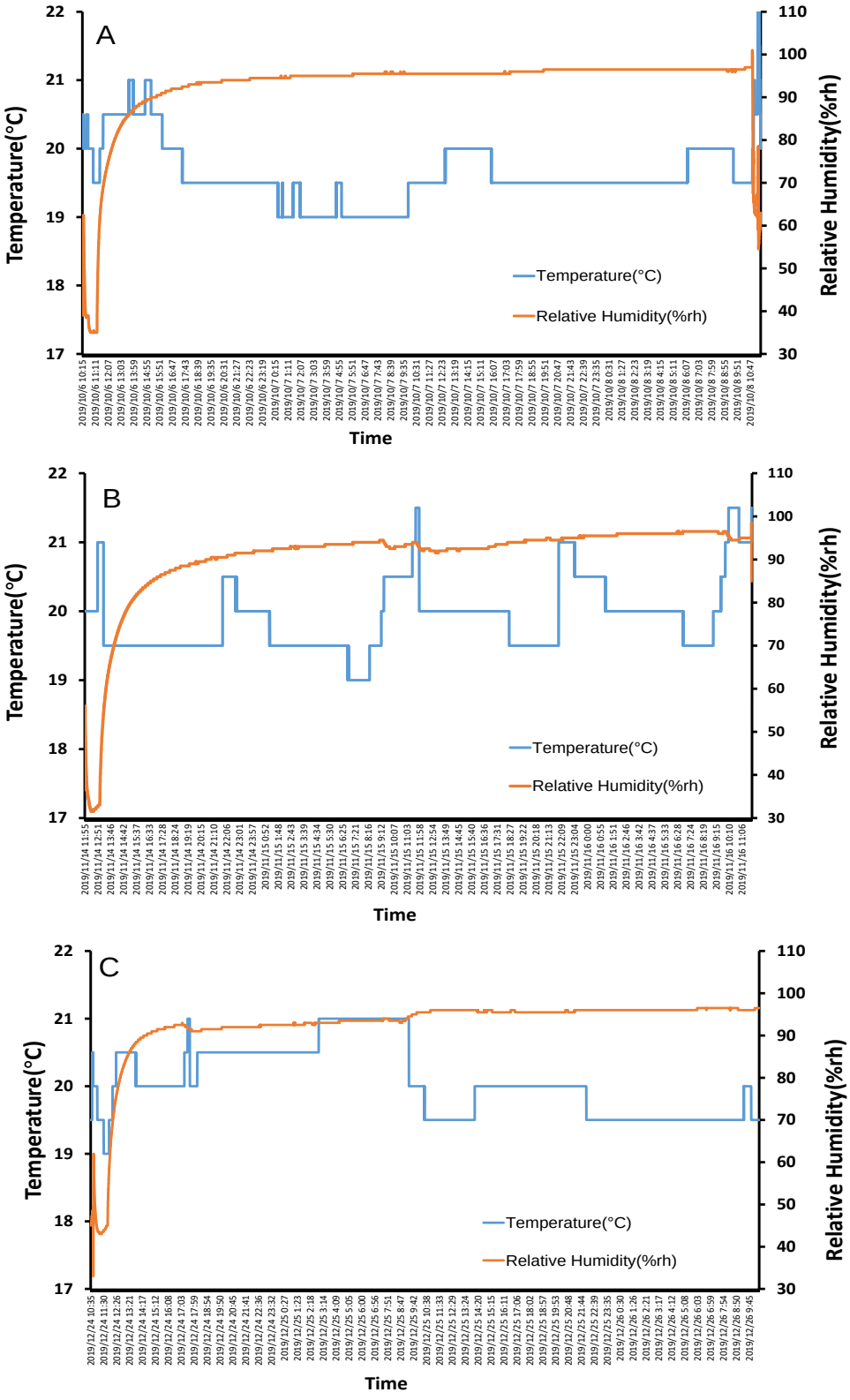

852

853 Figure S2. Temperature and relative humidity of the vacuum desiccator used for moisture
854 equilibrated samples preparation, A), B), C) corresponding to humidity experiments carried
855 out in triplicate.

856

Table S1. Fitting parameters for dual-site Langmuir model

Sample ID	α	$b_1(T)$	$b_2(T)$
K1-dry	0.16	0.016	0.5
K1-wet	0.011	0.021	0.2
K2-dry	0.15	0.016	0.43
K2-wet	0.0079	0.0091	0.9
SH1-dry	0.21	0.048	0.83
SH1-wet	0.0038	0.014	0.79
SH2-dry	0.19	0.034	0.53
SH2-wet	0.36	0.008	0.0082

$b_1(T)$ and $b_2(T)$ are the temperature-dependent equilibrium constants; $b_1(T)$ and $b_2(T)$ are weighted by a coefficient (α); α is the fraction of the second type of site ($0 < \alpha < 1$)